Energy & Environmental Science

ROYAL SOCIETY OF CHEMISTRY

PAPER

View Article Online
View Journal | View Issue

Cite this: *Energy Environ. Sci.*, 2023, **16**, 1548

Stability of solid electrolyte interphases and calendar life of lithium metal batteries†

Xia Cao, ‡[a] Yaobin Xu, ‡[b] Lianfeng Zou,[b] Jie Bao,[a] Yunxiang Chen,[c] Bethany E. Matthews,[a] Jiangtao Hu,[a] Xinzi He,[ad] Mark H. Engelhard,[b] Chaojiang Niu,[a] Bruce W. Arey,[a] Chunsheng Wang,[d] Jie Xiao,[ae] Jun Liu,[ae] Chongmin Wang, *[b] Wu Xu *[a] and Ji-Guang Zhang *[a]

Received 3rd November 2022,
Accepted 30th January 2023

DOI: 10.1039/d2ee03557j

rsc.li/ees

Lithium (Li) metal batteries (LMBs) are a promising candidate for next generation energy storage systems. Although significant progress has been made in extending their cycle life, their calendar life still remains a challenge. Here we demonstrate that the calendar life of LMBs strongly depends on the surface area of Li metal anodes exposed to the electrolyte and can be significantly improved by forming a stable solid electrolyte interphase (SEI) layer on the LMA surface. The stability and role of the accumulated SEI stacks are studied in their entirety in this work, beyond the conventional SEI investigations that focus on the local microscopic structure of a single SEI. Furthermore, we reveal, for the first time, the stability and reusability of this SEI during repeated lithium stripping/deposition processes using room temperature *in situ* electron microscopy. It is also demonstrated in this work that lithium anodes exhibit a much smaller active surface area under either fully charged or fully discharged conditions. Therefore, LMBs stored under these conditions exhibit a much longer calendar life than those stored at an intermediate state of charge. These findings reveal the most critical factors affecting the calendar life of LMBs and several approaches for improving both design and operation of these batteries to extend their calendar life have been proposed.

Broader context

The wide adoption of electric vehicles (EVs) around the world requires batteries with an energy density higher than those of the state-of-the-art lithium-ion batteries. In this regard, lithium (Li) metal batteries (LMBs) have been widely investigated as one of the most promising candidates for next generation high energy batteries for EVs. However, most studies on LMBs to date have focused on extending the cycle life of LMBs. Only very few studies have investigated their calendar life which is critical for EV applications which require a calendar life of more than 10 years. Herein, we reveal the most critical factors affecting the calendar life of LMBs and demonstrate an excellent calendar stability of LMBs by forming a robust and reusable solid electrolyte interphase (SEI) layer on the surface of a Li metal anode using an orthoformate based localized high concentration electrolyte. This electrolyte allows a high energy density LMB to retain 89.6% of its initial capacity after 18 months of storage in a fully discharged state. The stability and the role of the accumulated SEI stacks in their entirety have been investigated beyond the conventional SEI studies that focus on the local microscopic structure of an individual SEI layer. In addition, we also proposed several approaches to extend the calendar life of LMBs.

[a] *Energy and Environment Directorate, Pacific Northwest National Laboratory, Richland, Washington 99354, USA. E-mail: wu.xu@pnnl.gov, jiguang.zhang@pnnl.gov*
[b] *Environmental Molecular Sciences Laboratory, Pacific Northwest National Laboratory, Richland, Washington 99354, USA. E-mail: chongmin.wang@pnnl.gov*
[c] *Physical and Computational Sciences Directorate, Pacific Northwest National Laboratory, Richland, Washington 99354, USA*
[d] *Department of Chemical and Biomolecular Engineering, University of Maryland, College Park, MD 20742, USA*
[e] *Materials Science and Engineering Department, University of Washington, Seattle, Washington, 98195, USA*

† Electronic supplementary information (ESI) available: Fig. S1–S9: storage performance at elevated temperature, and Tables S1 and S2. Video S1 for *in situ* TEM recording of Li stripping. Video S2 for *in situ* TEM recording of Li replating. See DOI: https://doi.org/10.1039/d2ee03557j

‡ These two authors contributed equally to this work.

Introduction

Lithium (Li) ion batteries (LIBs) using graphite (Gr) as the anode and a broad range of cathode materials,[1,2] such as Li cobalt oxide (LCO) and Li nickel manganese cobalt oxide (NMC), have been an indispensable part of our daily life since the initial commercialization of Gr||LCO batteries in 1991.[3–6] With the eventual maturation of LIB technologies, a worldwide effort has recently been revitalized to develop batteries with higher specific energy densities, especially Li metal batteries (LMBs) using a Li metal anode (LMA).[7–11] Although the first rechargeable LMB consisting of an LMA and a titanium

disulfide (TiS_2) cathode was reported by Whittingham *et al.* of Exxon Enterprises in the 1970s,[5,12] the practical application of LMBs has been hindered due to safety concerns related to the growth of Li dendrites.[5,8,13,14] Since then, many new technologies and tools have been developed to address these concerns.[9,11,15,16] These approaches include new electrolyte development,[15–27] electrode engineering,[28] Li surface protection,[29,30] pressure control,[31] and advanced characterization techniques.[16] However, most of these studies focus on dendrite suppression and extending the cycle life of LMBs, while very limited research has been carried out on extending the calendar life of LMBs, which is also critical for application of these batteries, especially for use in electric vehicles (EVs), which need batteries with more than 10 years of calendar life.[32] The calendar life is the length of time for which a battery can be stored with limited use but still can recover at least 80% of its initial capacity, while the cycle life is the number of charge/discharge cycles a battery can undergo before it loses more than 20% of its initial capacity. Gr-based LIBs have demonstrated great calendar life (more than 10 years) and cycle life that enable their large-scale applications in EVs. In the case of silicon (Si)-based LIBs, although significant progress has been made in improving their cycle life, their calendar life still cannot satisfy the 10 year requirement for EV applications.[32,33] Similar challenges may also exist for LMBs, because both Si anodes and LMAs exhibit large volume changes during cycling, and newly exposed anode surfaces may have more side reactions with the electrolyte during storage. Recently, Boyle *et al.* investigated the corrosion of LMAs during the early stage of calendar aging (seven days).[34] They reported that Li||copper (Cu) half-cells lost about 2–3% of their capacities during a 24 hour storage period, even with some electrolytes that have demonstrated very high Li Coulombic efficiency, which can lead to a long cycle life of Li||Cu cells.[34] Therefore, there is an urgent need to systematically investigate the calendar life of LMBs and identify appropriate approaches that can help achieve both long cycling and long calendar life of LMBs for next-generation energy storage systems.

Calendar aging of LMBs is dominated by the formation (or accumulation) of solid electrolyte interphases (SEIs) on the surface of LMAs by side reactions of the electrolyte on the electrodes. Two key criteria for assessing the battery storage performance are the self-discharge rate (percentage of capacity loss per day in an open circuit) and recoverable capacity after long-term storage at a specified discharge rate which is directly related to the impedance of the batteries. Because metallic Li is highly reactive, the chemical stability of Li strongly depends on the protection of the SEI formed on its surface.[35] Recently, we developed a series of fluorinated orthoformate-based localized high concentration electrolytes (LHCEs) that can form a monolithic SEI on LMAs. This SEI is very homogeneous and enables long-term stable cycling of LMAs in high-voltage Li||$LiNi_{0.8}Mn_{0.1}Co_{0.1}O_2$ (NMC811) cells.[17,18] In this work, we systematically investigated the long-term calendar aging performance of Li||NMC811 cells using an LHCE at different states of charge (SOCs) (0%, 50%, and 100%) and two temperatures (30 °C and 55 °C).

Results and discussion

Reusable SEI shell structures

Suppression of Li corrosion is very critical to achieve a good calendar life of LMBs. Because Li has a redox potential of −3.040 V *vs.* the standard hydrogen electrode, which is beyond the stability window of the electrolyte, corrosion can easily occur on an LMA. A passivating SEI layer on the Li surface serves as a kinetic inhibitor, limiting continuous corrosion. Our previous studies demonstrated good cycling stability in Li||Li symmetric cells (Fig. S1a, ESI†) and Li||NMC811 cells (Fig. S1b, ESI†)[17,18] by using an advanced LHCE consisting of Li bis(fluorosulfonyl)imide (LiFSI), 1,2-dimethoxyethane and tris(2,2,2-trifluoroethyl) orthoformate (TFEO) at a molar ratio of 1 : 1.2 : 1. In particular, the highly homogeneous, monolithic SEI formed by this electrolyte prevents dendritic Li formation and minimizes Li loss and volumetric expansion during cycling.[17] Nevertheless, it is still difficult to fully eliminate Li corrosion by completely blocking electron transfer through the SEI layer. The LMA stability obtained during cycling may not reveal the true stability of an LMA during calendar aging.[34,36] Unlike a cycling test, where defects on the SEI can be quickly repaired during the repeated electrochemical charge/discharge processes, the SEI can hardly be patched during storage. As a result, Li corrosion caused by incomplete passivation could increase over time.

To investigate the calendar life of LMBs, Li||NMC811 coin cells (with a cathode loading of 4.2 mA h cm^{-2}, thin Li foil of 50 μm thickness, and a TFEO-based LHCE with an electrolyte/capacity ratio of 7 g $A^{-1}h^{-1}$) were charged to the target SOCs after two formation cycles in the voltage range of 2.8–4.4 V at C/10 (where 1C corresponds to 200 mA h g^{-1}, 4.2 mA cm^{-2}). As shown in Fig. 1a–c, cells were investigated at 30 °C under three SOC conditions, *i.e.*, at a fully discharged state (0% SOC, rest after formation cycles), a 50% charged state (50% SOC, with a specific capacity of 97 mA h g^{-1} charged at a constant current (CC) mode), and a fully charged state (where cells were charged to 4.4 V in the CC mode (100% SOC)). Scanning electron microscopy (SEM) images in Fig. 1d–i show the top and cross-sectional views of the three LMAs retrieved from these cells initially charged to the target SOCs. As shown in Fig. 1d and g, an SEI shell stack with pore structures (10–15 μm) accumulated on the LMA at 0% SOC, because the majority of the deposited Li had been stripped from the anode and intercalated into the cathode after two formation cycles, leaving an empty balloon-like SEI shell structure.

It is worth noting that the overall structure formed by the delithiated SEI shells has not fully collapsed even after Li has been almost completely removed because the SEI has good mechanical strength. This well-structured SEI stack is quite different from the SEI accumulation found on LMAs formed in conventional carbonate electrolytes, which is dominated by the randomly stacked, dendritic structure shown in ESI,† Fig. S2. Fig. 1j is a schematic illustration of the shell structure of the SEI stack at 0% SOC, which is formed by self-standing, nearly empty SEI shells. Only a very small amount of residual Li

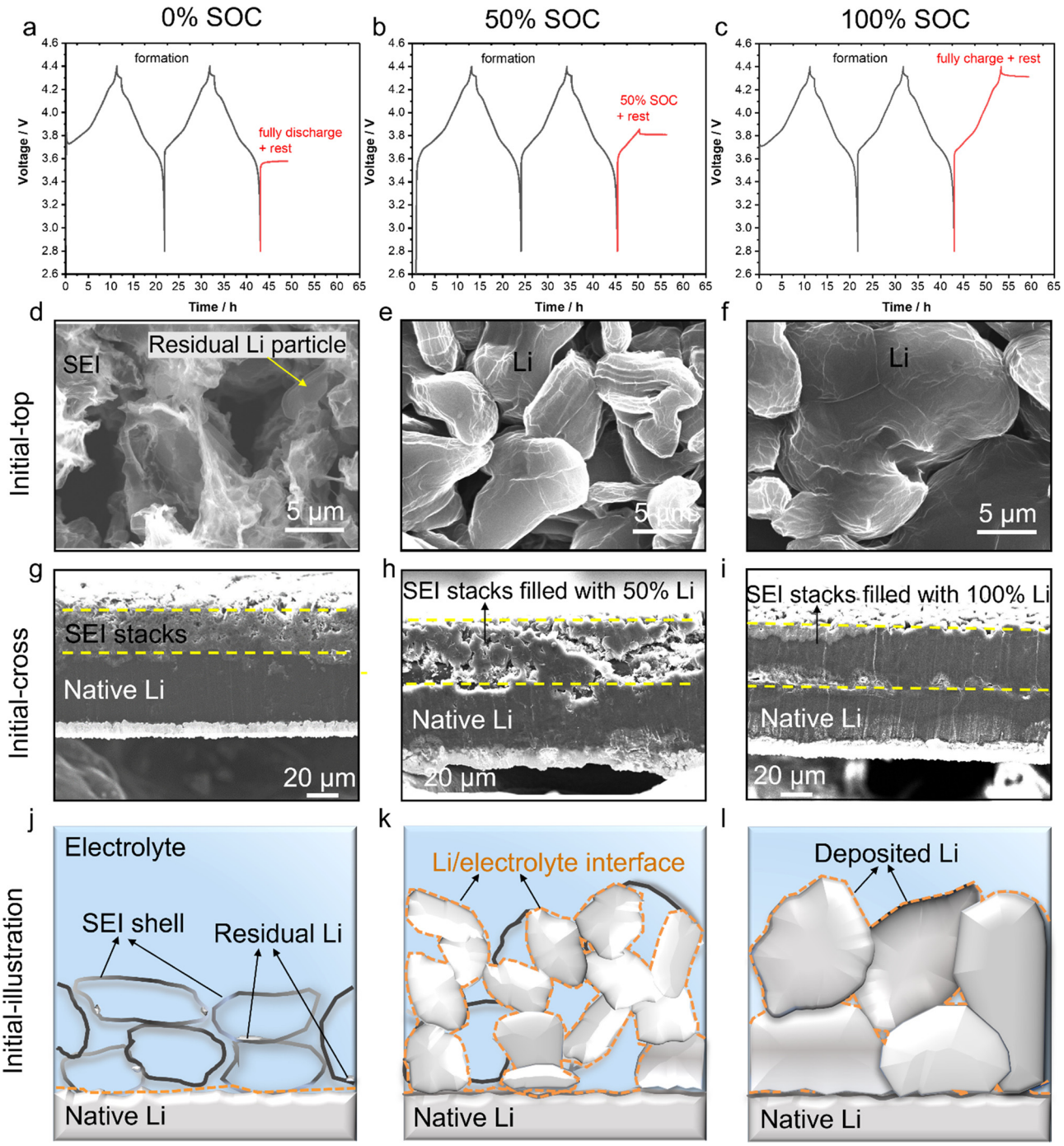

Fig. 1 Characteristics of LMAs during initial calendar aging test. (a–c) Voltage profiles of the cells during the formation process and rest conditions at target SOCs: (a) 0% SOC, (b) 50% SOC and (c) 100% SOC. (d–l) Li structure and SEI properties at initial states in Li||NMC811 cells at different SOCs. (d–f) Top, (g–i) cross-sectional views, and (j–l) schematic illustrations of SEM images of LMAs collected at the initial states of different SOCs after two formation cycles: (d, g and j) 0% SOC, (e, h and k) 50% SOC, and (f, i and l) 100% SOC.

particles remained in the SEI shells as shown in Fig. 1d. The residual Li left in the SEI shells can be a result of the increasing cell resistance when Li is continuously striped from the SEI stacks, and it is very difficult to completely remove all Li from these SEI stacks. The residual Li inside the SEI forms a natural electronic passage to facilitate Li deposition inside of the SEI balloons in the subsequent cycles. This well-maintained SEI structure greatly enhances its reusability during the subsequent Li plating process. SEM images of LMAs at 50% SOC (Fig. 1e and h) and 100% SOC (Fig. 1f and i) confirm this hypothesis. With the increases in SOC to 50% and 100%, the deposited Li from the cathode backfills the SEI shells and reuses the previously formed SEI films. In the case of 100% SOC, these balloon-like SEI shells are almost fully filled with Li, and the

bulky Li anode structure is shown in the cross-sectional view (Fig. 1i) and large Li grain particles (>10 μm) are observed in the top view (Fig. 1f). Corresponding schematic illustrations of the reacted layers for 50% SOC and 100% SOC are presented in Fig. 1k and l. The thickness change of the SEI shell stack indicates that the balloon-like SEI shells shrink when they are empty and expand when refilled with Li. Interestingly, the thickness of the Li anodes at 50% and 100% SOCs is similar, indicating that even a small portion of Li in the SEI shells can sustain the entire SEI shell structure.

An *in situ* transmission electron microscopy (TEM) study reveals, for the first time, the mechanical stability and reusability of the SEI shell structure formed on Li metal particles. It is known that the e-beam used in TEM probing of the SEI layer often leads to damage to the SEI layer. Therefore, cryo-TEM has been widely used to do *ex situ* investigation on the properties of an SEI layer at cryogenic temperature (<−170 °C).[37,38] However, it is impossible to use cryo-TEM to probe the *in situ* Li deposition and stripping process across the SEI layer. Recently, it has been reported that the electron dose rate, rather than the total electron dose, plays a critical role in imaging sensitive materials, such as Li and SEI layers. With a controlled electron dose rate (0.89 e^{-} $Å^{-2}$ s^{-1}), Li metal and SEI layers can be imaged at room temperature.[39] In this work, *in situ* TEM with a very low electron dose rate (0.33 e^{-} $Å^{-2}$ s^{-1}) was used to probe the Li stripping/deposition process across the SEI layer to avoid electron beam damage to Li and SEI layers at room temperature. Therefore, the electron beam damage to Li and SEI layers has been well mitigated. As shown in Fig. 2a, a randomly selected Li particle covered with an SEI shell, which was deposited on the Cu foil at 0.1 mA cm^{-2} for 1 hour in a Cu||NMC811 cell, was attached to a Cu wire for an *in situ* TEM study. By applying a bias voltage of 2.5 V (Pt as the negative electrode and Cu as the positive electrode), Li previously deposited inside the SEI shell on the Cu wire was gradually stripped out, and then deposited on the surface of the Pt electrode. This process is recorded in Video S1 (ESI†). A visible lighter/darker contrast boundary moves from the top-left corner to the bottom-right corner of the particle, which is caused by Li movement from the SEI shell to the Pt electrode. Fig. 2a–e show snapshots at different times during the Li stripping. The dashed yellow line is the contrast boundary line and indicates the Li stripping direction. After 782 seconds (Fig. 2c), the stripped Li can be observed on the Pt electrode, which grows continuously as more Li is stripped from SEI shell over time. After 3060 seconds (Fig. 2e), most of the Li previously stored inside the balloon-like SEI shell is deposited on the Pt electrode (at the top-right corner of the image, outside the SEI shell) as marked with a green arrow and the residual SEI becomes "empty". The images clearly show that the SEI shell does not fully collapse at the end of the Li stripping. Compared to the pristine Li particle, the residue SEI shell slightly shrinks, with an area decrease of 6.3% in the TEM image, as shown in Fig. 2e, where the green dashed circle indicates the size of the pristine particle, and the purple dashed line shows the edge of the residual SEI shell. Subsequently, by switching the positive and negative electrodes (Pt as the positive electrode and Cu as the negative electrode), the Li deposited on the Pt electrode gradually backfills into the SEI shell as shown in Fig. 2f–k, where the blue line indicates the Li replating border and direction. The green arrow shows the shrinkage of the Li that was previously deposited on the Pt electrode from the stripping process. At the end of the replating process (6125 seconds), all the Li deposited on the Pt electrode had moved back into the SEI shell, and the Li particle had almost the same shape and size as the pristine Li particle. Videos S2 (ESI†) shows the Li re-deposition process. This evidences that this SEI shell has great mechanical stability and can be reused in the subsequent Li plating and stripping processes. This is the first direct *in situ* observation of SEI shell reuse for an LMA. It also serves as a great example for studying the SEI as a self-sustained and complete structure instead of a local microscopic structure as reported in most of the previous works.

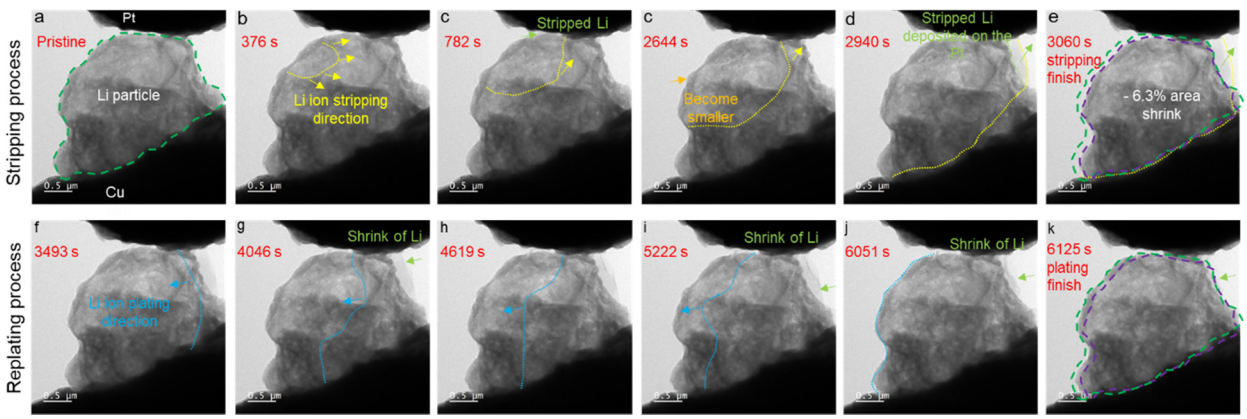

Fig. 2 Snapshots of the *in situ* TEM imaging during (a–e) Li stripping from the SEI shells to the Pt electrode (the dashed yellow line is the contrast boundary line and indicates the Li stripping direction) and (f–k) Li backfilling into SEI shells from the Pt electrode (the blue line indicates the Li replating border and direction). The green dashed circle indicates the size of the pristine particle, and the purple dashed circle indicates the size of the residual "empty" SEI shell.

Capacity recovery and self-discharge rates

This reusable SEI shell with high mechanical stability could largely improve the calendar life of LMBs. The electrochemical stability of fully assembled cells was tested by storing them at three SOCs for 18 months. As shown in Fig. 3a–d, cells were measured after selected storage periods (1 day, 1 week, 2 weeks, 3 weeks, 4 weeks, 5 weeks, 3 months, 6 months, 12 months, and 18 months) at 30 °C. At each scheduled time, cells stored at 0% SOC were charged and discharged at C/10 for 1 cycle to check the recoverable capacity, as shown in Fig. 3a. Cells stored at 50% or 100% SOC were first fully discharged at C/10 to check the capacity loss caused by self-discharge during the selected storage period, and then charged back to the target SOCs as shown in Fig. 3b and c. Generally, all the cells were very stable during storage. The recovered charge capacities after 18 months of storage are still close to their initial capacities. The highest discharge capacity retention was observed in the cells stored at 0% SOC, followed by those stored at 100% SOC and 50% SOC, where self-discharge was also involved. Table S1 (ESI†) summarizes the details derived from Fig. 3a–d.

For the cells stored at 30 °C at 0% SOC, the charge capacity gradually increased during the first 6 months from 204.8 to 225.4 mA h g^{-1} as a result of the cell activation (the initial 7 charge/discharge cycles). The discharge capacity also increased correspondingly in the first 3 months. However, it started to drop slightly after 3 month storage from the highest discharge capacity of 212.8 mA h g^{-1} obtained after 5 week storage. Thereafter, until the end of the 18 month storage, the discharge capacity was 181.9 mA h g^{-1}, which is 89.6% of the initial capacity (203.0 mA h g^{-1}) and 85.5% of the maximum capacity (212.8 mA h g^{-1}). This result clearly demonstrates that excellent capacity recovery can be achieved in high-voltage Li||NMC811 cells with the protection of the highly stable SEI formed by the advanced LHCE. The cells stored at 50% SOC were charged to a fixed specific capacity of 97 mA h g^{-1}. As shown in Table S1 (ESI†), the discharge capacity slightly decreased in the first 3 months of storage. Dividing the capacity loss by the storage time and the charging capacity, the self-discharge rates obtained for different periods were between 0.19% per day and 0.82% per day. The average self-discharge rate for the first 6 months of storage was 0.42%/day. After another 6 months of storage, from 12 months to 18 months, all of the 97 mA h g^{-1} charging capacity was lost by self-discharge.

For the cells stored at 100% SOC, the charging capacity also slightly increased because of the cell activation (the initial 6 cycles). A minimum self-discharge capacity of about 10 mA h g^{-1} was observed after the first 5 weeks, and a discharge capacity of 105 mA h g^{-1} was observed at the end of 18 months of storage. Overall, the self-discharge rates were between 0.02%/day and 1.38%/day during different time periods, with an average self-discharge rate of 0.24%/day. Results for cells stored at 100% SOC with an additional constant voltage (CV) charge step at 4.4 V are shown in Fig. S3 (ESI†) and are summarized in Table S2 (ESI†) compared to the cells stored at 100% SOC without a CV step. The storage performance at 100% SOC with a CV step followed the same trend as

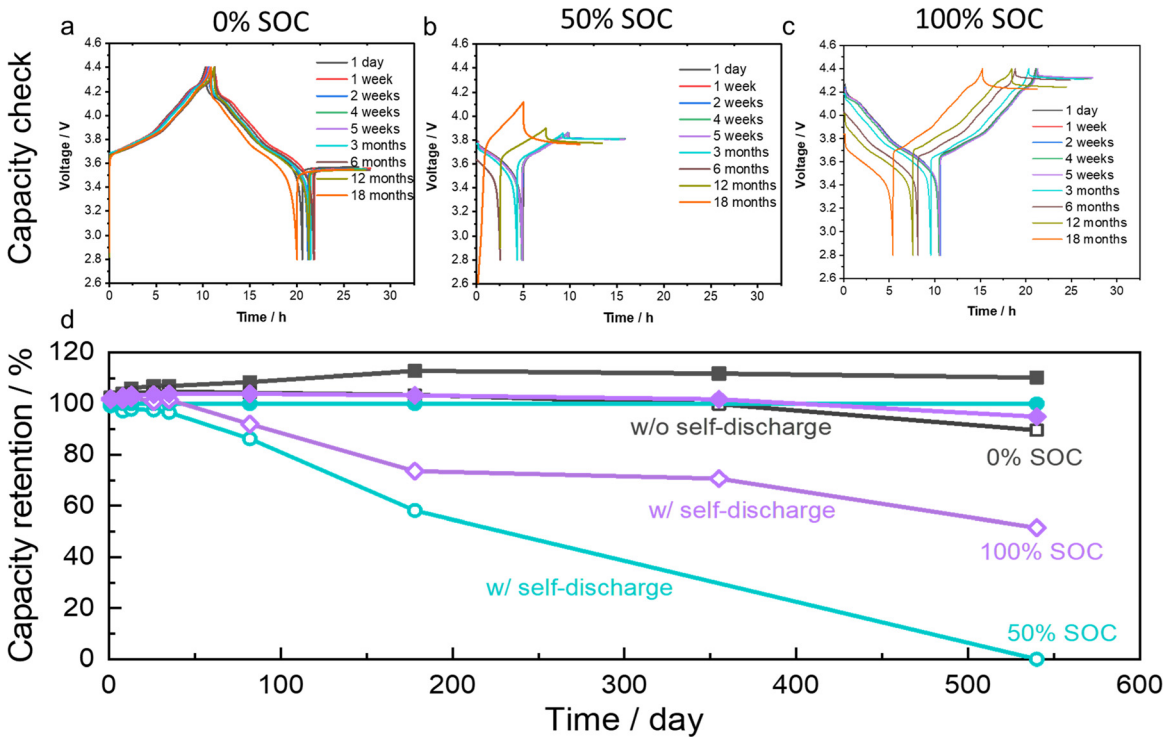

Fig. 3 Electrochemical performance of the cells stored at different SOCs at 30 °C. (a–c) Voltage profiles of the cells during the storage after different elapsed times within 18 months of storage at 30 °C at (a) 0% SOC, (b) 50% SOC, and (c) 100% SOC. (d) Capacity retention of the cells stored at different SOCs as a function of storage time; solid symbols are used for charge capacity and open symbols for discharge capacity.

that of the cells stored at 100% SOC without CV, but capacities were slightly increased with the CV charge step. Two parallel cells were also evaluated to check the repeatability of the tests, as shown in Fig. S4 (ESI†). These parallel cells exhibited similar voltage profiles during storage tests. In particular, for the first 12 months, the voltage profiles of the two parallel cells are almost overlapped. The calendar aging stability of LMBs observed in this work is very promising for practical applications of LMBs.

Delineating the factors affecting the calendar aging

To better understand the cell storage behaviors, the electrodes were collected from the Li||NMC811 cells after 18 months of storage for postmortem analysis. Photographs of the opened cells that had been stored at different SOCs are shown in Fig. S5 (ESI†). Overall, the cell stored at 0% SOC was in the best condition, while uneven Li deposition is evident in the cell stored at 50% SOC and the separator of the cell stored at 100% SOC has a brownish tint. The morphology of the corresponding LMAs stored at different SOCs for 18 months is shown in Fig. 4a–c (cross-sectional views) and in Fig. S6 (top views), ESI.† The sustainability of the stacked SEI shells is further evident from the well-maintained Li morphology after long-term storage. In the cells stored at 0% SOC, the SEI shell structure was maintained after 18 months of storage (Fig. S6, ESI†), and ~45 μm of native Li (with metal luster) remained in the cells (Fig. 4a), which can be easily distinguished from the SEI accumulated on the top of the native Li. Since the Li metal foil was initially 50 μm thick, only about 10% of the Li degraded during the 11 interim capacity-check cycles and 18 month storage, which corresponds to a minimum degradation rate of 0.018%/day. This stability can be attributed to the solid protection of the SEI shells, which minimize the geometric Li surface area exposed to electrolyte, as illustrated in Fig. 1j.

In the case of the cells stored at 100% SOC, the SEI shells are almost completely filled with the Li coming from the cathode (Fig. 4c and Fig. S6e, f, ESI†). Hence, the Li/electrolyte interface is mainly present on the top of the LMA and there is only trace electrolyte residue left in the reacted Li layer, as illustrated in Fig. 1l. Therefore, the Li corrosion in cells stored at 100% SOC is also limited to the top surface because the bulk Li is already protected by SEI shells, and the reacted Li remains in a bulky structure with a minimal exposure to electrolyte during 18 months of storage. However, in the case of the cells charged to 50% SOC, only half of the SEI shells are filled with Li, forming loosely distributed Li that can be eventually penetrated by electrolyte. Unlike the dense, bulky deposited Li found at 100% SOC, this deposited Li at 50% SOC exposes a much more Li surface to the electrolyte, as illustrated in Fig. 1k. To quantify the difference between Li deposited at 50% SOC and 100% SOC, a Cu current collector with deposited Li was transferred into a Thermo Fisher Helios 5 Hydra DualBeam plasma focused ion beam scanning electron microscope (PFIB-SEM) to acquire 3D slicing images (72 pieces) at every 100 nm at cryogenic temperature. These images were then stacked, with the assistance of a standard image segment assembly process and machine learning, to reconstruct a 3D structure of the deposited Li. The geometry of the Li particles in cells stored at 50% and 100% SOC is shown in Fig. 4d and e, respectively. The volumetric Li fraction is 40.3% in the reacted Li layer for the Li deposited at 50% SOC and 91.9% for the Li deposited at 100% SOC, meaning 59.7% of the volume of the 50% SOC sample consists of SEI films and pores, while this value is only 8.1% for the 100% SOC sample. Therefore, the Li deposited in the cell stored at 50% SOC has a much larger surface area exposed to the electrolyte than that in the cell stored at 100% SOC. As a result, Li corrosion is accelerated in the cell stored at 50% SOC. This is in good agreement with the electrochemical performance, as shown in Fig. 3. In addition, the SEI composition of the LMA after 18 months of storage was also systematically investigated. The atomic ratios of seven elements in the SEI in cells stored at different SOCs are compared in Fig. 4f. High Li and O atomic ratios are found on the SEIs obtained under all three conditions, meaning that all SEIs are dominated by inorganic (Li_2O_x) components, especially for the 0% SOC condition, under which the fewest side reactions took place. Very similar compositions of SEIs are found under 50% SOC and 100% SOC conditions. This observation further suggests that the Li/electrolyte interface area (Li anode porosity) is a critical factor that determines the self-discharge rate during storage. In addition, a trace amount of transition metal (Ni) is found on the LMA stored at 100% SOC, indicating that slight Ni dissolution occurs when the cathode is stored in a fully charged state.

Fig. 5a–i compares the morphologies and structures of cathode particles retrieved from Li||NMC811 cells. Apparently, the structure of NMC811 spherical secondary particles is well maintained without any cracking after 18 months of storage at all SOCs, as shown in Fig. 5a–c, where SEM images were obtained by focused ion beam milling combined with scanning electron microscopy (FIB-SEM). High-angle annular dark-field scanning transmission electron microscopy (HAADF-STEM, Fig. 5d–f) and annular bright-field STEM (ABF-STEM, Fig. 5g–i) disclose the atomic-level changes in the cathode structure. The pristine NMC811 exhibits a clear layered structure and could experience structural reconstruction during cycling and calendar aging due to the interactions between the electrolyte and NMC811. In this work, the cathode structure reconstruction during calendar aging is quantified. For the NMC811 stored at 0% SOC, a thin (~1.5 nm) rock salt reconstruction layer (outlined by red dashed lines), where certain anti-site Ni ions occupy the Li sites, exists on the surface of NMC811 primary particles (Fig. 5d). With the higher SOCs of 50% and 100%, the reconstruction layers become slightly thicker, namely, 2.7 nm (Fig. 5e) and 6.1 nm (Fig. 5f), respectively. This indicates that the detrimental phase transition was accelerated at 100% SOC, with a degradation rate that is four times that found at 0% SOC. This accelerated detrimental effect can be attributed to the increased catalytic activity of transition metals like Ni^{4+} at high voltages. The same trend is found at the cathode electrolyte interphase (CEI), which is derived from the electrolyte decomposition products, and is outlined by the yellow dashed lines in Fig. 5g–i, the ABF-STEM images. The CEI thickness increased

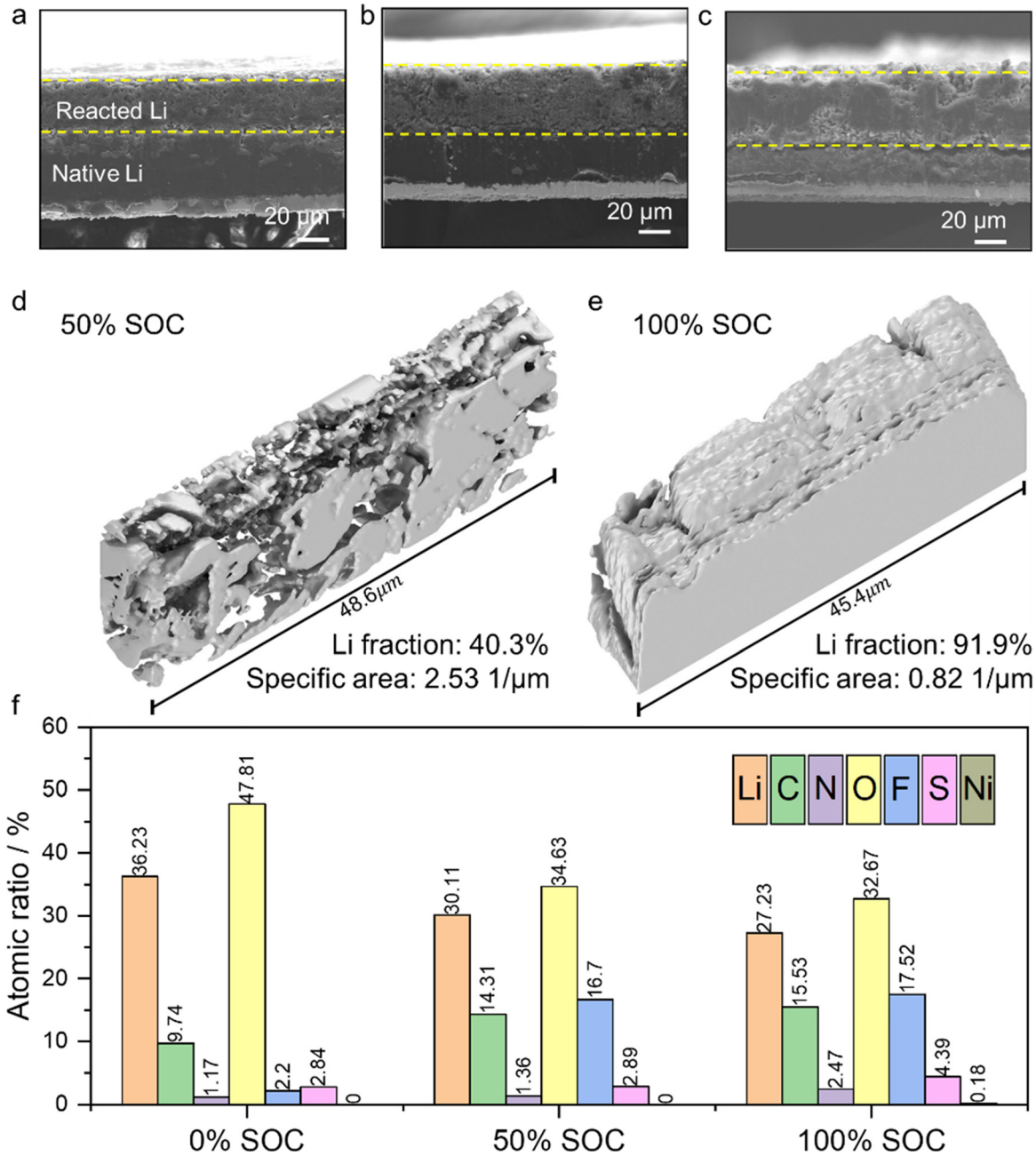

Fig. 4 Structure of Li anode in Li||NMC811 cells after 18 months of storage at 30 °C and at different SOCs. (a) Cross-sectional SEM images of Li anodes retrieved from cells stored at 0% SOC, (b) 50% SOC, and (c) 100% SOC. (d and e) Reconstructed 3D Li structures of Li metal collected from cells stored at (d) 50% SOC and (e) 100% SOC. (f) X-ray photoelectron spectroscopy results (elemental distribution) of SEIs on the Li anodes after 18 months of storage at different SOCs at 30 °C.

from 1.5 nm to 2.0 nm and 3.2 nm at SOCs of 0%, 50%, and 100%, respectively, suggesting a stronger interaction between NMC811 and electrolyte during storage at higher SOCs. Fig. S7 (ESI†) shows the structure of the NMC811 cathode collected in the cell stored at 100% SOC with additional CV charge at 4.4 V; it is similar to the NMC structure of cells stored at 100% SOC without CV charge.

The thinness of the structural reconstruction layer and CEI layer after 18 months of storage is very encouraging. In particular, the <4 nm CEI and <7 nm NMC811 structural reconstruction layer after 18 months of storage at 100% SOC clearly indicate that the CEI formed in this TFEO-based LHCE effectively protects the NMC811 cathode from severe side reactions between the electrolyte and the cathode. Hence, the cathode degradation can also be excluded as the dominant reason for the cell deterioration during calendar aging. In addition, this understanding of cathode degradation during calendar aging will also greatly help simplify the quantification of the effect of SOC on cell cycling; it could minimize the influence of many other variables in the charge or discharge

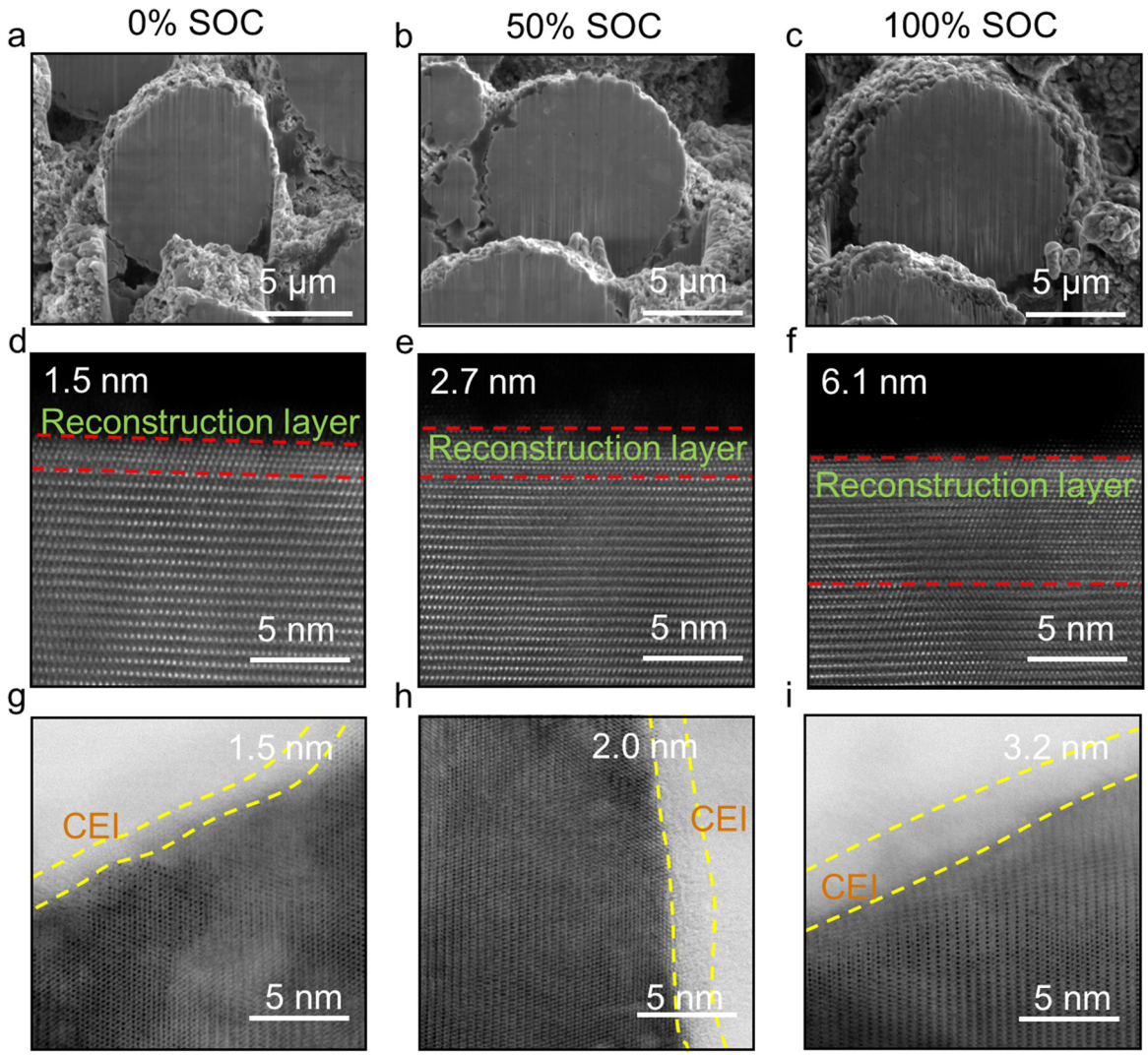

Fig. 5 Structural and CEI properties of the NMC811 particles in Li||NMC811 cells after 18 months of storage at 30 °C at different initial SOCs. (a–c) FIB-SEM, (d–f) HAADF-STEM and (g–i) annular bright-field (ABF)-STEM images of NMC811 cathodes retrieved from cells stored at (a, d and g) 0% SOC, (b, e and h) 50% SOC, and (c, f and i) 100% SOC.

profiles, including the time span at high voltage, current density, and electrode polarization.

The degradation of Li||NMC811 cells was further investigated by storing the cells at 55 °C for up to 18 months as shown in ESI,† Fig. S8a–c. The calendar life of Li||NMC811 cells stored at 55 °C follows the same order of 0% SOC > 100% SOC > 50% SOC that was observed at 30 °C; it also correlates with the rankings of the porosities and surface areas of the Li deposited in cells stored at 50% SOC > 100% SOC > 0% SOC. More defects at SEIs were observed over the long-term storage at 55 °C while defects at the SEI are negligible at 30 °C. Therefore, storage at elevated temperature is detrimental to the calendar life of LMBs.

Cycling stability of the cell after 18 months of storage

Based on the voltage profiles obtained from cells stored at different SOCs and temperatures, storage at 0% SOC and 30 °C is the preferable storage condition for LMBs. After 18 months of storage, the cell stored under this optimal condition was further evaluated with a cycling test. As shown in ESI,† Fig. S8d, the stored cell showed a faster capacity decay than the fresh cell that also used the LHCE. Its capacity retention was 44.0% after 100 cycles, while it was 93.6% for the fresh cell with the LHCE in the same cell setup. A fresh cell using commercial electrolyte 1.2 M $LiPF_6$ in ethylene carbonate and ethyl methyl carbonate (3 : 7 by wt.) with 2% vinylene carbonate as an additive was also used as a reference. Fewer than 10 cycles can be achieved in this cell under the same testing conditions, which is much poorer than the cells using the LHCE, even when the cell using a LHCE has been stored for 18 months. These results further evidence the great Li metal stability provided by the protection of the robust and reusable SEI shells formed in the LHCE.

Conclusions

A systematic long-term calendar-life study of LMBs was performed in this work. Li||NMC811 cells with a fluorinated

orthoformate-based LHCE demonstrated a highly stable calendar life at 30 °C as revealed by the periodic measurement of self-discharge rates and capacity recovery during long-term storage. 89.6% of initial capacity can be recovered after 18 months of storage at 0% SOC. Very low average self-discharge rates of 0.42%/day and 0.24%/day were observed in the cells stored at 50% and 100% SOC, respectively. A thin reconstruction layer on the NMC811 cathode structure (1.5 nm thick) and minimum LMA consumption (5 μm) were found after 18 months of storage at 0% SOC. These results demonstrate great potential for the long-term calendar life of high-voltage LMBs. Moreover, these systematic studies revealed the fundamental mechanism that controls the calendar life of Li anodes and LMBs at the nano and micro levels during long-term calendar aging. Li degradation, rather than NMC811 deterioration, is the dominant factor that determines the calendar life of LMBs. An SEI shell structure with good mechanical strength can sustain repeated Li plating/stripping with minimal structural failure. This is the key for the extended calendar life of LMBs using this advanced LHCE. 50% SOC is a less favorable storage condition because the deposited Li is highly porous, exposing a large Li/electrolyte interface area; the best storage condition is 0% SOC, followed by 100% SOC storage because Li anodes stored under these conditions have a much less surface area exposed to the electrolyte. These findings provide clear guidance for further development of LMBs with both extended cycle life and long calendar life.

Experimental

Electrolyte and electrode preparation, cell assembly, and testing

The TFEO-based electrolyte was prepared by dissolving LiFSI salt in a solvent mixture of DME and TFEO at a ratio of 1 : 1.2 : 1 by mol. inside an MBraun glovebox filled with purified argon (Ar), where the moisture and oxygen content were less than 1 ppm. LiFSI was received from Nippon Shokubai Co., Ltd (Tokyo, Japan) and used after drying at 120 °C in a vacuum for 24 hours. DME (battery grade) was obtained from Gotion, Inc. (Fremont, CA, USA) and used as received. TFEO was purchased from SynQuest Laboratories (Alachua, FL, USA) and dried with pre-activated 4 Å molecular sieves for 5 days prior to use. 50 (±2) μm thick Li on Cu foil (China Energy Lithium, Co., Ltd, Tianjin, China) was used as the anode. The $Ni_{0.8}Mn_{0.1}Co_{0.1}O_2$ (NMC811) electrode comprising 96 wt% NMC811, 2 wt% Super C65 carbon and 2 wt% polyvinylidene fluoride was used as the cathode with a capacity loading of 4.2 mA h cm^{-2}. Li||NMC811 CR2032 coin cells were assembled for the calendar life test, in which a piece of the NMC811 electrode (1.27 cm diameter), a piece of the polyethylene separator (Asahi Hi-Pore, Japan) (1.90 cm diameter), and a piece of Li (1.50 cm diameter) were sandwiched together with 37.5 μL of electrolyte (7 g $A^{-1}h^{-1}$). An Al-clad positive case (EQ-CR2032-CASE-AL, MTI, a positive case made of stainless-steel 304 with Al coating) was used in this work to minimize corrosion of the regular stainless-steel positive case at high voltage. An additional Al foil (1.90 cm) was placed in between the cathode disk and the Al-clad positive case to further deter corrosion of the positive case. The Li||NMC811 cells were activated by two formation cycles within a voltage range of 2.8–4.4 V at C/10 charge and discharge rates, where 1C was 200 mA g^{-1} (~4.2 mA cm^{-2}). The cells were then charged to the target SOCs: fully discharged (0% SOC, rest directly after full discharge at the end of formation cycles), 50% SOC (97 mA h g^{-1} charge capacity at C/10) and fully charged (100% SOC, charged to 4.4 V at a current density of C/10 (with or without a constant voltage at 4.4 V until current reached C/20)). the capacity recovery and self-discharge rates were monitored over different storage times (1 day, 1 week, 2 weeks, 4 weeks, 5 weeks, 3 months, 6 months, 12 months and 18 months) at 30 °C and 55 °C. Cells stored at 0% SOC were used to check the capacity recovery. After each time interval, the cell was fully charged and fully discharged, and the capacity recovery was calculated by dividing this discharge capacity by the initial capacity (discharge capacity after the second formation cycle). Cells stored at 50% SOC and 100% SOC were first fully discharged to 2.8 V to measure the capacity loss since their previous charge and then charged back to 50% SOC or 100% SOC, as appropriate. The self-discharge rate was calculated by dividing the measured capacity loss by the previously charged capacity and the storage time. The average self-discharge rate for the entire test was obtained by dividing the sum of capacity losses by the whole storage time.

In situ TEM characterization

In this work, *in situ* TEM with a very low electron dose rate (0.33 e^- $Å^{-2}$ s^{-1}) has been used to probe the Li stripping/deposition process across the SEI layer during *in situ* TEM observation to avoid electron beam damage to Li and SEI at room temperature.[39] A Cu||Li cell with a TFEO based LHCE electrolyte was used to deposit the Li particles for the *in situ* TEM tests. After the electrochemical deposition at 0.1 mA cm^{-2} for 1 hour, the coin cells were disassembled inside an argon-filled glovebox to avoid reaction of the deposited Li with the air. The Cu electrode deposited with Li was taken out of the battery and rinsed with DME solvent three times to remove residual electrolyte and then dried under vacuum for 20 min to remove residual DME. After that, a Cu wire was used to collect a deposited Li particle covered with the SEI (which is loosely distributed on the Cu substrate due to low-capacity Li deposition). Then the Cu wire with deposited Li covered with an SEI layer was loaded to a nanofactory-STM holder inside a glovebox, and on another side Pt wire was used as the working electrode. The holder was then covered with an Ar-filled bag and transferred to a 300 kV FEI Titan monochromated (scanning) transmission electron microscope equipped with a probe aberration corrector. Inside the transmission electron microscope, the Cu wire with deposited Li working as a counter electrode was manipulated using a piezoelectric positioning system on the holder to contact the Pt wire. Then a constant bias of 2.5 V was applied between the two electrodes. Under a constant driving force for Li stripping, the Li ions migrated across the SEI layer and diffused to the Pt wire. Subsequently, by switching the bias between the two electrodes, the Li deposited on the Pt

electrode gradually backfills into the SEI shell. The Li stripping and replating process was recorded with a charge-coupled device.

Postmortem characterization

For postmortem analyses of the stored cells, including SEM, FIB-SEM, and TEM measurements, long-term stored Li||NMC811 cells were disassembled inside a glovebox to collect the LMAs and the NMC811 cathodes. Each electrode was rinsed with 1 mL of DME solvent to remove the residual electrolyte and then vacuum dried before being sealed in airtight containers in the glovebox and being transferred for further characterization. The cross-sections of the NMC811 particles were cut with a gallium (Ga) ion beam (accelerating voltage of 30 kV and current of 2.5 nA) and polished (current of 0.43 nA) to obtain the cross-sectional images of the NMC811 particles. For TEM sample preparation, a 300 nm platinum layer and a 3 μm carbon layer were coated on the NMC811 particles, which were randomly selected for the lift-out processes. Ion beams were set at 30 kV and 5 kV to thin the particle, and then at 2 kV to further polish the surface and remove the damaged layers. These FIB-SEM and TEM sample preparations were performed on an FEI Helios Nanolab 660 DualBeam Ga FIB-SEM system. The as-prepared TEM sample was then characterized by a standard procedure on a JEOL JEM-ARM200CF spherical-aberration-corrected microscope as described in our previous work.[40] The top and cross-sectional view SEM images of the cross-sections of the LMAs were recorded on a JEOL JSM-IT200 system at an accelerating voltage of 15 kV. 3D slicing using focused ion beam was carried out to reconstruct the 3D Li structure of cells charged at 50% SOC and 100% SOC after two formation cycles in Li||NMC811 cells. Each Li metal anode was mounted on an SEM stub inside a glovebox, and then this SEM stub was transferred to a Thermo Fisher Helios 5 Hydra DualBeam system (plasma focused ion beam scanning electron microscope (PFIB-SEM)) *via* an inert gas transfer system to avoid air contamination. After that, the SEM stage was cooled to −190 °C and 3D-slice images were acquired at cryogenic temperature. This process was performed using Thermo Fisher Auto Slice & View 4 software.

Image process

The raw cryo-FIB-SEM images cannot be directly reconstructed into 3-dimensional microstructures because the gray scales of Li on the SEM images are not identical. Therefore, a standard image segmentation process was implemented on the original SEM images to identify and separate the Li from background (other materials and pores). This consists of four main steps. (1) Before the segmentation, the original SEM images were preprocessed for smoothing by a fast, nonlocal denoising method.[41] (2) The non-background (Li) and background pixels were approximately separated by a simple gray threshold. (3) The non-background pixels were converted to an L*A*B* color space[42] for finer classification. Bilateral filtering was conducted for the color channels "L," "A," and "B" for categorizing the L*A*B* color into two clusters using the mini-batch *K*-means algorithm.[43] (4) Multi-stage image processes, such as small pixel removal, erosion, dilation, and nonlocal denoising were conducted to finalize the identification and separation of Li. A new binary labeled picture then was created for pixels on each SEM image, where value 1 stands for Li and value 0 for background. Because some of the FIB-SEM images have inconsistent quality, the standard segmentation steps mentioned above might not have provided satisfying Li identification results. Therefore, a machine-learning-based segmentation convolutional neural network (SCNN) was applied to enhance the Li separation quality for some of the SEM images with inconsistent brightness, contrast, and sharpness. The SCNN's structure followed the one introduced by Sciazko *et al.*[44] for a 256 × 256-pixel patch. The original SEM images with acceptable quality were used as training inputs, and the corresponding binary labeled pictures, which labeled the Li pixels, were used as the training output data. The trained SCNN was then used to identify Li for the SEM images with inconsistent brightness, contrast, and sharpness. After applying the standard and machine-learning-based segmentation approaches mentioned above, adequate continuous binary labeled pictures for Li were collected for the remaining images. The binary pictures were then stacked slice-by-slice into 3-dimensional microstructure data, in which value 1 stands for Li and 0 for background. The geometry of the Li particles for 50% and 100% SOC is shown in Fig. 4d and e, respectively, in the manuscript, which is the isosurface for a labeling value of 0.5.

Author contributions

J.-G. Z., W. X., and X. C. proposed the research and designed the experiments. X. C. performed the electrochemical measurements and conducted SEM observations with help from X. H. Y. X. and C. W. performed *in situ* TEM. J. B. and Y. C. reconstructed the 3D Li structure, M. E. performed XPS, and J. H., L. Z., B. E. M., B. W. A. and C. W. performed FIB and TEM. C. N. prepared the NMC811 electrodes. X. C., W. X., and J.-G. Z. prepared the manuscript with input from all other coauthors.

Conflicts of interest

There are no conflicts to declare.

Acknowledgements

This work is supported by the Assistant Secretary for Energy Efficiency and Renewable Energy in the Vehicle Technologies Office of the U.S. Department of Energy (DOE) through the Advanced Battery Materials Research program (Battery500 Consortium) under contract no. DE-AC05-76RL01830. XPS, FIB-SEM and TEM were conducted in the William R. Wiley Environmental Molecular Sciences Laboratory, a national scientific user facility sponsored by DOE's Biological and Environmental Research program and located at Pacific Northwest National Laboratory (PNNL). PNNL is operated by Battelle

for the DOE under Contract DE-AC05-76RL01830. The LiFSI salt was provided by Nippon Shokubai Co., Ltd.

References

1 N. Nitta, F. Wu, J. T. Lee and G. Yushin, *Mater. Today*, 2015, **18**, 252–264.
2 M. S. Whittingham, *Chem. Rev.*, 2004, **104**, 4271–4302.
3 J. B. Goodenough and K. S. Park, *J. Am. Chem. Soc.*, 2013, **135**, 1167–1176.
4 M. Li, J. Lu, Z. Chen and K. Amine, *Adv. Mater.*, 2018, **30**, 1800561.
5 M. S. Whittingham, *Proc. IEEE*, 2012, **100**, 1518–1534.
6 M. Winter, B. Barnett and K. Xu, *Chem. Rev.*, 2018, **118**, 11433–11456.
7 D. Lin, Y. Liu and Y. Cui, *Nat. Nanotechnol.*, 2017, **12**, 194.
8 J. Liu, Z. Bao, Y. Cui, E. J. Dufek, J. B. Goodenough, P. Khalifah, Q. Li, B. Y. Liaw, P. Liu, A. Manthiram, Y. S. Meng, V. R. Subramanian, M. F. Toney, V. V. Viswanathan, M. S. Whittingham, J. Xiao, W. Xu, J. Yang, X.-Q. Yang and J.-G. Zhang, *Nat. Energy*, 2019, **4**, 180–186.
9 C. Niu, H. Lee, S. Chen, Q. Li, J. Du, W. Xu, J.-G. Zhang, M. S. Whittingham, J. Xiao and J. Liu, *Nat. Energy*, 2019, **4**, 551–559.
10 M. M. Thackeray, C. Wolverton and E. D. Isaacs, *Energy Environ. Sci.*, 2012, **5**, 7854–7863.
11 W. Xu, J. Wang, F. Ding, X. Chen, E. Nasybulin, Y. Zhang and J.-G. Zhang, *Energy Environ. Sci.*, 2014, **7**, 513–537.
12 M. S. Whittingham, *J. Electrochem. Soc.*, 1976, **123**, 315–320.
13 D. Aurbach and Y. Cohen, *J. Electrochem. Soc.*, 1996, **143**, 3525–3532.
14 J. B. Goodenough and Y. Kim, *Chem. Mater.*, 2010, **22**, 587–603.
15 N. Piao, X. Ji, H. Xu, X. Fan, L. Chen, S. Liu, M. N. Garaga, S. G. Greenbaum, L. Wang, C. Wang and X. He, *Adv. Energy Mater.*, 2020, **10**, 1903568.
16 A. J. Louli, A. Eldesoky, R. Weber, M. Genovese, M. Coon, J. deGooyer, Z. Deng, R. T. White, J. Lee, T. Rodgers, R. Petibon, S. Hy, S. J. H. Cheng and J. R. Dahn, *Nat. Energy*, 2020, **5**, 693–702.
17 X. Cao, X. Ren, L. Zou, M. H. Engelhard, W. Huang, H. Wang, B. E. Matthews, H. Lee, C. Niu, B. W. Arey, Y. Cui, C. Wang, J. Xiao, J. Liu, W. Xu and J.-G. Zhang, *Nat. Energy*, 2019, **4**, 796–805.
18 X. Cao, L. Zou, B. E. Matthews, L. Zhang, X. He, X. Ren, M. H. Engelhard, S. D. Burton, P. Z. El-Khoury, H.-S. Lim, C. Niu, H. Lee, C. Wang, B. W. Arey, C. Wang, J. Xiao, J. Liu, W. Xu and J.-G. Zhang, *Energy Storage Mater.*, 2021, **34**, 76–84.
19 S. Chen, J. Zheng, D. Mei, K. S. Han, M. H. Engelhard, W. Zhao, W. Xu, J. Liu and J.-G. Zhang, *Adv. Mater.*, 2018, **30**, 1706102.
20 X. Ren, L. Zou, X. Cao, M. H. Engelhard, W. Liu, S. D. Burton, H. Lee, C. Niu, B. E. Matthews, Z. Zhu, C. Wang, B. W. Arey, J. Xiao, J. Liu, J.-G. Zhang and W. Xu, *Joule*, 2019, **3**, 1662–1676.
21 Y. Yamada and A. Yamada, *J. Electrochem. Soc.*, 2015, **162**, A2406–A2423.
22 J. Holoubek, M. Yu, S. Yu, M. Li, Z. Wu, D. Xia, P. Bhaladhare, M. S. Gonzalez, T. A. Pascal, P. Liu and Z. Chen, *ACS Energy Lett.*, 2020, **5**, 1438–1447.
23 J. Chen, Q. Li, T. P. Pollard, X. Fan, O. Borodin and C. Wang, *Mater. Today*, 2020, **39**, 118–126.
24 Z. Yu, H. Wang, X. Kong, W. Huang, Y. Tsao, D. G. Mackanic, K. Wang, X. Wang, W. Huang, S. Choudhury, Y. Zheng, C. V. Amanchukwu, S. T. Hung, Y. Ma, E. G. Lomeli, J. Qin, Y. Cui and Z. Bao, *Nat. Energy*, 2020, **5**, 526–533.
25 Y. Yang, Y. Yin, D. M. Davies, M. Zhang, M. Mayer, Y. Zhang, E. S. Sablina, S. Wang, J. Z. Lee, O. Borodin, C. S. Rustomji and Y. S. Meng, *Energy Environ. Sci.*, 2020, **13**, 2209–2219.
26 X. Ren, P. Gao, L. Zou, S. Jiao, X. Cao, X. Zhang, H. Jia, M. H. Engelhard, B. E. Matthews, H. Wu, H. Lee, C. Niu, C. Wang, B. W. Arey, J. Xiao, J. Liu, J.-G. Zhang and W. Xu, *Proc. Natl. Acad. Sci. U. S. A.*, 2020, **117**, 28603–28613.
27 X. Cao, P. Gao, X. Ren, L. Zou, M. H. Engelhard, B. E. Matthews, J. Hu, C. Niu, D. Liu, B. W. Arey, C. Wang, J. Xiao, J. Liu, W. Xu and J.-G. Zhang, *Proc. Natl. Acad. Sci. U. S. A.*, 2021, **118**, e2020357118.
28 G. Zheng, S. W. Lee, Z. Liang, H.-W. Lee, K. Yan, H. Yao, H. Wang, W. Li, S. Chu and Y. Cui, *Nat. Nanotechnol.*, 2014, **9**, 618–623.
29 C. Wang, Y. S. Meng and K. Xu, *J. Electrochem. Soc.*, 2019, **166**, A5184–A5186.
30 J. Lopez, A. Pei, J. Y. Oh, G.-J. N. Wang, Y. Cui and Z. Bao, *J. Am. Chem. Soc.*, 2018, **140**, 11735–11744.
31 C. Fang, B. Lu, G. Pawar, M. Zhang, D. Cheng, S. Chen, M. Ceja, J.-M. Doux, M. Cai, B. Liaw and Y. Meng, *Nat. Energy*, 2021, **6**, 987–994.
32 B. Cunningham, presented in part at the **https://www.energy.gov/eere/vehicles/2020-vehicle-technologies-office-amr-presentations-program**, 2020.
33 J. D. McBrayer, M.-T. F. Rodrigues, M. C. Schulze, D. P. Abraham, C. A. Apblett, I. Bloom, G. M. Carroll, A. M. Colclasure, C. Fang, K. L. Harrison, G. Liu, S. D. Minteer, N. R. Neale, G. M. Veith, C. S. Johnson, J. T. Vaughey, A. K. Burrell and B. Cunningham, *Nat. Energy*, 2021, **6**, 866–872.
34 D. T. Boyle, W. Huang, H. Wang, Y. Li, H. Chen, Z. Yu, W. Zhang, Z. Bao and Y. Cui, *Nat. Energy*, 2021, **6**, 487–494.
35 E. Peled and S. Menkin, *J. Electrochem. Soc.*, 2017, **164**, A1703–A1719.
36 D. Lin, Y. Liu, Y. Li, Y. Li, A. Pei, J. Xie, W. Huang and Y. Cui, *Nat. Chem.*, 2019, **11**, 382–389.
37 Y. Li, Y. Li, A. Pei, K. Yan, Y. Sun, C.-L. Wu, L.-M. Joubert, R. Chin, A. L. Koh and Y. Yu, *Science*, 2017, **358**, 506–510.
38 X. Wang, Y. Li and Y. S. Meng, *Joule*, 2018, **2**, 2225–2234.

39 W. Zhai, B. Yuan, Y. Fan, Y. Zhang, X. Zhang, Y. Ma, W. Liu and Y. Yu, *J. Am. Chem. Soc.*, 2022, **144**, 4124–4132.
40 L. Zou, Z. Liu, W. Zhao, H. Jia, J. Zheng, Y. Yang, G. Wang, J.-G. Zhang and C. Wang, *Chem. Mater.*, 2018, **30**, 7016–7026.
41 V. Karnati, M. Uliyar and S. Dey, Fast Non-Local algorithm for image denoising, *2009 16th IEEE International Conference on Image Processing (ICIP)*, Cairo, Egypt, 2009, pp. 3873–3876, DOI: **10.1109/ICIP.2009.5414044**.
42 *International Commission on Illumination (CIE)*, ed. E. C. Carter, Y. Ohno, M. R. Pointer, A. R. Robertson, R. Sève, J. D. Schanda and K. Witt, Colorimetry, CIE, 3rd edn, 2004, vol. 15, p. 72, ISBN: 9783901906336.
43 D. Sculley, presented in part at the Proceedings of the 19th international conference on World wide web, Raleigh, North Carolina, USA, 2010.
44 A. Sciazko, Y. Komatsu, T. Shimura and N. Shikazono, *J. Electrochem. Soc.*, 2021, **168**, 044504.